Journal of Rare Earths 41 (2023) 250–258

Contents lists available at ScienceDirect

Journal of Rare Earths

journal homepage: http://www.journals.elsevier.com/journal-of-rare-earths

One-step solution combustion synthesis of micro-nano-scale porous Cu/CeO_2 with enhanced photocatalytic properties[☆]

Zhichao Shang [a, b], Yong Yu [a], Hang Yang [a], Zhongxiang Yang [a], Yang Xiao [c, **], Xiaohong Wang [a, *]

[a] *School of Materials Science and Physics, China University of Mining and Technology, Xuzhou 221116, China*
[b] *School of Chemical Engineering and Technology, China University of Mining and Technology, Xuzhou 221116, China*
[c] *Davidson School of Chemical Engineering, Purdue University, West Lafayette, IN, 47907-2100, USA*

ARTICLE INFO

Article history:
Received 9 October 2021
Received in revised form
7 February 2022
Accepted 22 February 2022
Available online 5 March 2022

Keywords:
Solution combustion synthesis
Cu/CeO_2
Nanoporous material
Photocatalyst
Rare earths

ABSTRACT

The Cu/CeO_2 nanoporous composite material was prepared via a one-step and energy-saving method of solution combustion synthesis (SCS). The phase composition, surface morphology and optical characteristics of Cu/CeO_2 were studied. The results show that the SCS products are composed of cubic fluorite CeO_2 and Cu. Due to the generation and escape of gas during the synthetic reaction, the SCS CeO_2 shows porous structure, in which the mesopores (diameter 10–17 nm) nest in the wall of large pores (diameter 80–300 nm). X-ray photoelectron spectroscopy (XPS) outcomes indicate that the oxygen vacancy concentration of CeO_2 increases (18.97%–30.93%) with the increase of Cu concentration. The decoration of Cu greatly enhances the catalytic activity of CeO_2 nanomaterials. 30 wt% Cu/CeO_2 composite material shows the best photocatalytic activities for the degradation of methyl orange (MO) (95.99%), which is about 4.3 times that of CeO_2 at the same time (120 min). UV-vis diffuse reflectance spectroscopy (DRS) results show that the semiconductor band gap is reduced with the addition of metallic Cu, which leads to the enhancement of photocatalytic activity. The free radical trapping experiments demonstrate that $\cdot O_2^-$ and h^+ are the main active species in the photocatalytic degradation of MO. Based on the above results, a hypothesized mechanism for enhanced photocatalysis of Cu/CeO_2 nanomaterials was proposed: the porous structure provides more reactive sites and channels for mass transfer, and the presence of metallic Cu improves the oxygen vacancy concentration of CeO_2 and then promotes charge-carrier separation, which helps enhance the photocatalytic performance of Cu/CeO_2.

1. Introduction

There are more than 105 dyes on the commercially dyes with over 7 × 10^5 t produced by textile, printing, and paper industries annually.[1] Various methods have been utilized to remove organic pollutants from aqueous environments such as adsorption,[2] coagulation and flocculation,[3] ion exchange and electrochemical methods,[4] etc. Most of the above remediation techniques are not only costly but also have complicated operation processes, and may produce harmful by-products of aromatic amines.[5] Photocatalysis is a way of material conversion by using light energy. It generates holes and hydroxyl radicals under light to completely oxidize and degrade organic pollutants in wastewater. Cerium, which accounts for 0.0046 wt% of the earth's crust, is the most abundant rare earth element,[6] and its oxidation state possesses excellent thermal stability, chemical stability. As a stable rare-earth oxide, CeO_2 has attracted a lot of attention on account of its high mobility of the oxygen species and reversible conversion from Ce^{4+} and Ce^{3+}, which makes it have excellent redox and oxygen storage capacity.[7] So it is cheap and widely used in cosmetics, fuel cells, sensors, etc.[8–10] Besides, it is very important in the field of photocatalysis. Zou et al. used CeO_2 hybridized C_3N_4 to enhance the photocatalytic hydrogen evolution of visible light[11]; Wang et al. increased the photocatalytic performance of CeO_2 catalysts to reduce CO_2 to H_2O with the irradiation of simulated sunlight produced by Fe-doped CeO_2 catalysts[12]; Zhong et al. prepared hollow CeF_3 nanospheres

---

[☆] **Foundation item:** Project supported by the Fundamental Research Funds for the Central Universities (2019ZDPY20) and Postgraduate Research & Practice Innovation Program of Jiangsu Province (KYCX21_2199).

[*] Corresponding author.
[**] Corresponding author.
E-mail addresses: xiao63@purdue.edu (Y. Xiao), wxhcumt@cumt.edu.cn (X. Wang).

https://doi.org/10.1016/j.jre.2022.02.013
1002-0721/

co-doped with activator Tm^{3+} and sensitizer Yb^{3+} for photocatalytic nitrogen fixation.[13]

Nevertheless, because of the wide band gap of CeO_2 (~3.2 eV), the low utilization rate of sunlight and fast recombination efficiency of electron-hole, the application of CeO_2 in wastewater treatment has been limited. Surface modification of CeO_2 with metal makes it useful and effective to better the photocatalytic performance of CeO_2. For example, Li et al. employed the oxygen vacancy and the synergism between Ni and CeO_2 to enhance the catalyst activity in the phenol gasification[14]; Negi et al. modified CeO_2 with Ag to improve its photocatalytic performance and achieved approximate 100% degradation of Rhodamine B (RhB) dye in 150 min.[15] Among them, Cu-modified CeO_2 nanomaterials have received widespread attention because of their low cost and high natural abundance. Also, the introduction of Cu in CeO_2 further improves the reversible redox cycle, effectively suppresses electron-hole coincidence, and increases oxygen storage vacancies.[16–18]

Till now, Cu-CeO_2 has been synthesized in various methods, such as hydrothermal, precipitation bonding, microwave, and solid-state. Channei et al. synthesized Cu-doped cerium dioxide nanoparticles by combining homogeneous precipitation with impregnation methods[19]; Azizi et al. doped 5 wt%–20 wt% copper into CeO_2 nanostructures by a sonochemical method, and the performance of the synthesized catalyst was evaluated via the degradation of MO.[20] The preparation methods in the above reports are all completed in a two-step or multi-step process (CeO_2 is first prepared, and Cu is loaded by other technologies.). Compared with the above technologies, solution combustion synthesis (SCS) is an efficient preparation method, which uses the self-propagating exothermic reaction between reactants for material synthesis without the addition of any surfactants or extra chemicals.[21,22] In addition, the SCS method does not need special and expensive equipment, and has been used to synthesize thousands of nanomaterials, such as NiO, CuO, Bi_2O_3, etc.[23–25] And some metals or metal/oxide composite (Ni, Ag/CeO_2, etc.) could also be synthesized via SCS in one step. However, there is no relevant report on the one-step preparation of Cu/CeO_2.

Herein, a series of Cu-decorated CeO_2 composites were successfully prepared in one step by the modified solution combustion synthesis method. And then the structure and photocatalytic properties of the as-synthesized catalysts were characterized. The loading of Cu affects the recombination rate of carriers and the concentration of oxygen vacancies (OVs) in the CeO_2 photocatalyst, and made it exhibit a significantly lower band gap than that of CeO_2. Moreover, the photocatalytic degradation performance of Cu/CeO_2 nanomaterials was investigated through the degradation of MO, and a feasible mechanism was proposed in combination with the trapping experiment. This work provides an easy and convenient way to synthesize a photocatalyst for the treatment of wastewater.

2. Experimental

2.1. Materials and synthesis

All the following raw materials were obtained from Aladdin Chemical Reagent Co., Ltd., China, and were used directly without further purification: cerium nitrate hexahydrate ($Ce(NO_3)_3\cdot 6H_2O$, AR), tartaric acid (L-$C_4H_6O_6$, ACS), copper nitrate trihydrate ($Cu(NO_3)_2\cdot 3H_2O$, AR), and Methyl Orange (MO, AR).

Cu/CeO_2 photocatalysts powders were prepared via solution combustion synthesis method in argon atmosphere. The reaction of $Ce(NO_3)_3\cdot 6H_2O$ and L-$C_4H_6O_6$ can be represented as Eq. (1); and the reaction between $Cu(NO_3)_2\cdot 3H_2O$ and L-$C_4H_6O_6$ is identified as Eq. (2).

$$Ce(NO_3)_3\cdot 6H_2O + \frac{7}{5}C_4H_6O_6 = CeO_2 + \frac{3}{2}N_2 + \frac{28}{5}CO_2 + \left(\frac{21}{5} + 6\right)H_2O \tag{1}$$

$$Cu(NO_3)_2 + \frac{6}{5}C_4H_6O_6 = CuO + CO + \frac{19}{5}CO_2 + \frac{18}{5}H_2O + N_2 \tag{2}$$

In a typical SCS procedure, 2.17 g $Ce(NO_3)_3\cdot 6H_2O$, 0.98 g $Cu(NO_3)_2\cdot 3H_2O$, and 1.78 g $C_4H_6O_6$ were dissolved in 10 mL deionized water (DIW) with magnetic stirring for 10 min at 353 K. The obtained homogeneous colloidal liquid was transferred into a quartz boat and heated at 600 °C in the argon-filled tubular furnace for 30 min. This sample was labeled A4 (30 wt% Cu). Other samples denoted as A1, A2 and A3 (CeO_2, 10 wt% Cu and 20 wt% Cu) according to the weight ratio of Cu/CeO_2 were synthesized using the same steps. The amounts of reagents are listed in Table 1. The reaction process of Cu/CeO_2 is shown in Fig. S1.

2.2. Characterization

The crystalline phase composition and structures of the as-prepared CeO_2 and Cu/CeO_2 were analyzed by powder X-ray diffraction (XRD, Bruker D8 advance, Germany) in the 2θ ranging from 20° to 80°. The microstructures and elemental composition of as-prepared samples were explored by a field emission scanning electron microscope with energy dispersive spectroscopy (FE-SEM, Hitachi SU8220, Japan). The morphology and size of the Cu/CeO_2 were characterized via high-resolution transmission electron microscopy (HRTEM, TecnaiG2 F20, USA) with the nickel grid as the powder supporter. The chemical states of CeO_2 and Cu were determined by X-ray photoelectron spectroscopy (XPS, Escalab 250Xi, USA) with Al Kα radiation source. The charging effect on as-prepared samples was compensated via binding energies referenced to 284.8 eV of C 1s' peak. The specific surface area, average pore diameter, and total pore volume of the Cu/CeO_2 composites were characterized using N_2 gas Brunauer-Emmett-Teller analysis (BET, BELSORP-max, Japan). And the pore size distribution curves were characterized from the adsorption and desorption branches based on the Barrett-Joyner-Halenda (BJH) method.

The optical properties were analyzed via a UV-vis spectrophotometer (Lambda 750 s, USA) at 554 nm, and the photoluminescence (PL, FLS980, UK) spectra were recorded by applying a 325 nm excitation. And the photochemical properties of the as-prepared photocatalytic materials were determined by using a three-electrode chemistry apparatus (CHI-760E, China). The transportability of photo-generated electrons and holes in photocatalysis was investigated by testing the transient photocurrent response of the products in ten lights on/off cycles.

Table 1
The amounts (g) of reagents for each sample.

Samples	Solution A		Solution B	
	$Ce(NO_3)_3\cdot 6H_2O$	$C_4H_6O_6$	$Cu(NO_3)_2\cdot 3H_2O$	$C_4H_6O_6$
A1	2.17	1.05	0	0
A2 (10 wt% Cu)	2.17	1.05	0.32	0.24
A3 (20 wt% Cu)	2.17	1.05	0.65	0.48
A4 (30 wt% Cu)	2.17	1.05	0.98	0.73

2.3. Photocatalytic performance

In each experiment, 50 mg sample was dropped to MO aqueous solution and stirred in the dark for 30 min to maintain uniform suspension and achieve adsorption/desorption equilibrium. Then, under the irradiation of the visible light source, 5 mL was taken every 20 min and centrifuged to remove the photocatalyst. Next, the change of dye concentration in the solution was characterized by UV-Vis spectroscopy. The efficiency of catalytic degradation was calculated according to Eq. (3):

$$\text{Catalytic efficiency} = \left(\frac{A_0 - A_\text{i}}{A_0}\right) \times 100\% \tag{3}$$

where A_i denotes the MO solution concentration after degradation, while A_0 represents the initial concentration of MO solution.

3. Results and discussion

3.1. Phase constitution and structural properties

Fig. 1 presents the X-ray diffraction patterns of CeO_2 samples and Cu/CeO_2 nanoparticles. The presence of sharp peaks in the XRD patterns manifests that the SCS products have good crystallinity. For products A1 (CeO_2), the major peaks at $2\theta = 28.55°$, 33.08°, 47.48°, 56.33°, 59.09°, 69.40°, 76.70° and 79.07° can be assigned to the cubic fluorite structure of CeO_2 (JCPDS 34–0394). And the three new peaks at $2\theta = 43.29°$, 50.43°, and 74.13° as shown in the XRD patterns of Cu/CeO_2 are indexed to the cubic Cu (JCPDS 04-0836), manifesting the existence of metal Cu in the composites.

In order to obtain metal Cu, extra fuel of tartaric acid and argon atmosphere was used, resulting in a reductive environment. As shown in Eq. (2), in the "copper nitrate tartaric acid" system, CuO is formed at the early stage of the reaction, and then CuO is reduced to metal Cu by the reducing gas (CO) released from fuel decomposition (Eq. (4)). In addition, CeO_2 is a stable oxide that is difficult to be reduced by CO.

$$CuO + CO = Cu + CO_2 \tag{4}$$

Moreover, the relative height of the Cu diffraction peaks becomes higher with the increase of the Cu amount. Based on the XRD patterns, the crystalline grain size (D) of A1, A2, A3 and A4 were calculated as 5.3, 6.1, 3.7 and 4.4 nm, respectively, utilizing the Scherrer equation[26] (Eq. (5)).

$$D = \frac{K\lambda}{\beta \cos \theta} \tag{5}$$

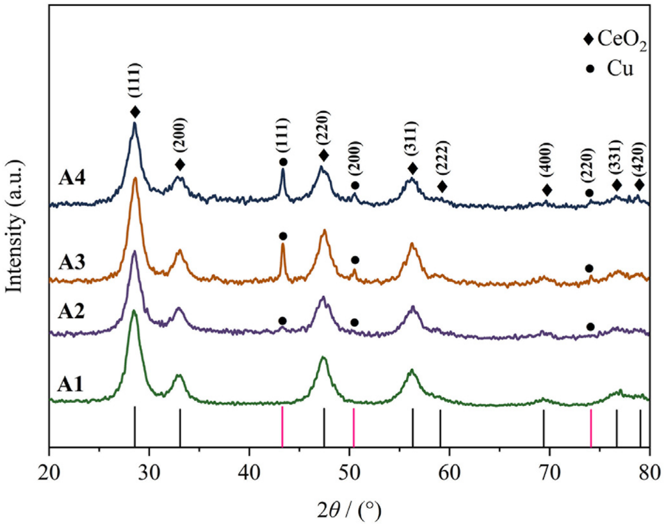

Fig. 1. XRD patterns of CeO_2 and Cu/CeO_2 composites.

Fig. 2(a, c) is the SEM micrographs of the SCS CeO_2, showing that the as-prepared CeO_2 (Fig. 2(a)) is composed of many irregular nano flake-like structures. A further observation from high-magnification images (Fig. 2(c)) reveals a porous structure, in which the CeO_2 crystalline grains form as the skeleton and two kinds of pores appear in it. The diameter of the large pores is around 80–300 nm, while the mesopores, which nested in the wall of the large pores, are only 10–17 nm. The generation of these pores can be ascribed to the production and escape of gas during the synthetic reaction. According to Eq. (1), the production of 1 mol CeO_2 is accompanied by the production of 7.1 mol of gas. Fig. 2(b, d) are the SEM images of 30 wt% Cu/CeO_2 (A4) at different magnifications, which also exhibit similar porous structures with large pores and mesopores. The BET (see Fig. S2) surface area of the 30 wt% Cu/CeO_2 composites is measured to be 23.42 m^2/g, which is less than that of the CeO_2 (33.21 m^2/g). And the pore volume of 0.082 cm^3/g is slightly reduced compared with CeO_2 (0.093 cm^3/g). The EDS map (Fig. 2(e–h)) shows that Cu, Ce, and O elements are uniformly distributed throughout the sample, which indicates that Cu is evenly decorated on the CeO_2 matrix.

From the TEM images (Fig. 3) of the 30 wt% Cu/CeO_2 composite, it can be seen that this sample is composed of many spherical nanoparticles, whose diameters ranging from 3.3 to 7.8 nm. The HRTEM image (Fig. 3(b)) exhibits well-crystallized lattice fringes of the SCS Cu/CeO_2 composite. Fig. 3(b) is an enlarged version of the box of Fig. 3(a), in which the lattice fringes with a plane spacing of 0.204 nm correspond to the (111) crystal plane of the face-centered cubic (fcc) Cu phase, while the lattice spacing (0.268 nm) is matched well with the (200) crystal plane of CeO_2. In a nutshell, the HRTEM observations are highly identical with the XRD results and the FESEM energy spectrum results, which further illustrates the successful synthesis of Cu-decorated CeO_2 composites via the one-step SCS method.

The detailed chemical state and bonding environment of the as-synthesized photocatalytic materials were made certain via using XPS (Fig. 4). The charging effect on the as-prepared samples was compensated via binding energies referenced to 284.8 eV of C 1s' peak. The XPS survey spectra of Cu/CeO_2 are shown in Fig. 4(a). And Fig. 4(b) shows the high-resolution XPS spectra of Ce 3d of all the as-synthesized composite nanomaterials. It is obvious that all the Ce 3d spectra of all samples could be divided into four pairs of spin-orbital splitting bimodal peaks, and cerium exists in the mixed-valence states of the Ce element.[27] The resolved binding energies at 882.1, 888.4, 897.9, 900.7, 907.5 and 916.4 eV[28,29] are indicative of Ce^{4+} 3d state,[30,31] while the other peaks (884.6 and 903.4 eV) present characteristic of Ce^{3+} 3d state.[32] Compared with pure CeO_2, the electron binding energy peaks of Ce species in 10 wt% Cu/CeO_2, 20 wt% Cu/CeO_2 and 30 wt% Cu/CeO_2 composite nanomaterials slightly shift toward high electron binding energy, indicating that the chemical environment of Ce species in Cu/CeO_2 composite nanomaterials changes with the increase of Cu loading.[33] Whereas, in terms of the XRD results, cerium exists as CeO_2 in the tetravalent state, and without diffraction peaks of Ce_2O_3, which implies that trivalent cerium ions exist in the crystal lattice of CeO_2. The existence of Ce^{3+} in CeO_2 crystalline will induce the lattice distortion and generate more oxygen vacancies in the CeO_2 crystalline.

For the sake of comparing the Ce^{3+} concentration in CeO_2 before and after Cu loading, the area of fitted peaks was calculated by Eq. (6) (the results are listed in Table S1).

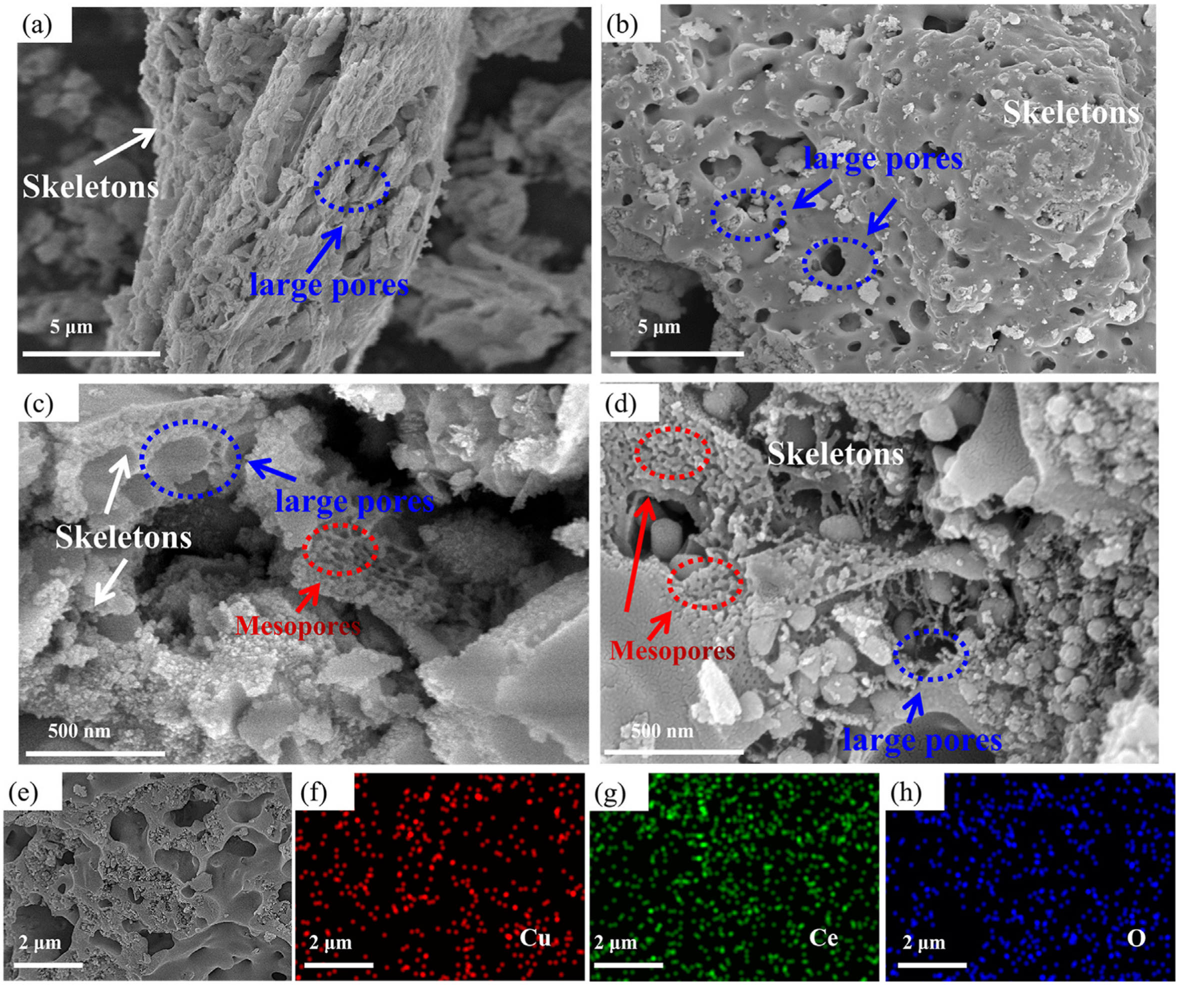

Fig. 2. SEM images of CeO_2 (a, c) and 30 wt% Cu/CeO_2 (b, d); EDS mapping images of CeO_2 (e) and for Cu (f), Ce (g) and O (h) of the 30 wt% Cu composite.

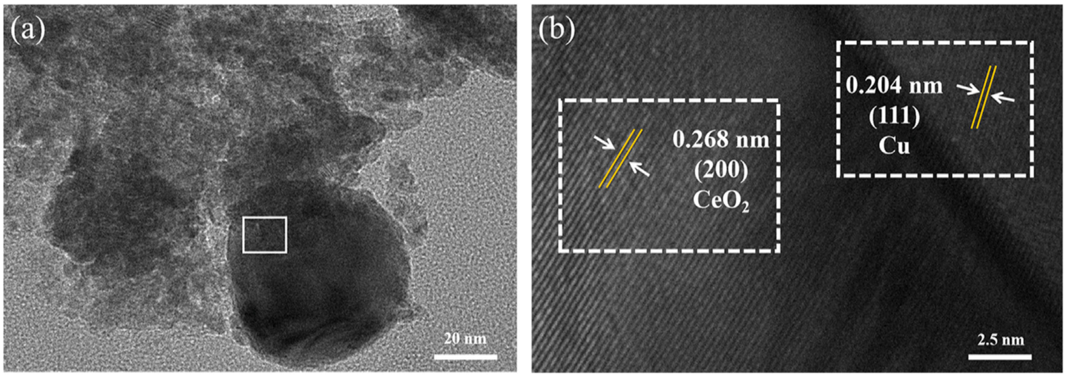

Fig. 3. TEM (a) and HRTEM (b) images of the 30 wt% Cu composite.

$$C_{\mathrm{Ce}^{3+}} = \frac{\mathrm{Ce}^{3+}}{\mathrm{Ce}^{3+} + \mathrm{Ce}^{4+}} \tag{6}$$

where $\mathrm{Ce}^{3+} = U_1 + V_1$ and $\mathrm{Ce}^{4+} = U + U_2 + U_3 + V + V_2 + V_3$ (Fig. 4(b)). Sample A4 shows the highest C_{Ce}^{3+} value (30.93%), followed by A3 (27.53%) and A2 (25.57%). And A1 material had the lowest C_{Ce}^{3+} value (only 18.97%), which means that the percentages of Ce^{3+} ions are highly dependent on the Cu content. Higher Ce^{3+} concentration in CeO_2 will induce more OVs, which will promote the electron transfer process, effectively prevent the charge carriers' recombination, and help to enhance the photocatalytic activity.[34] Due to the addition of copper nitrate and tartaric acid in the reaction system, the reaction environment is in a fuel-rich state. The reduction of Cu^{2+} to Cu (Eq. (4)) was achieved during the combustion of the fuel-rich system due to the reducing environment created by the product gases (CO),[35] and part of the tetravalent cerium ions are also reduced to trivalent (Eq. (7)). And then,

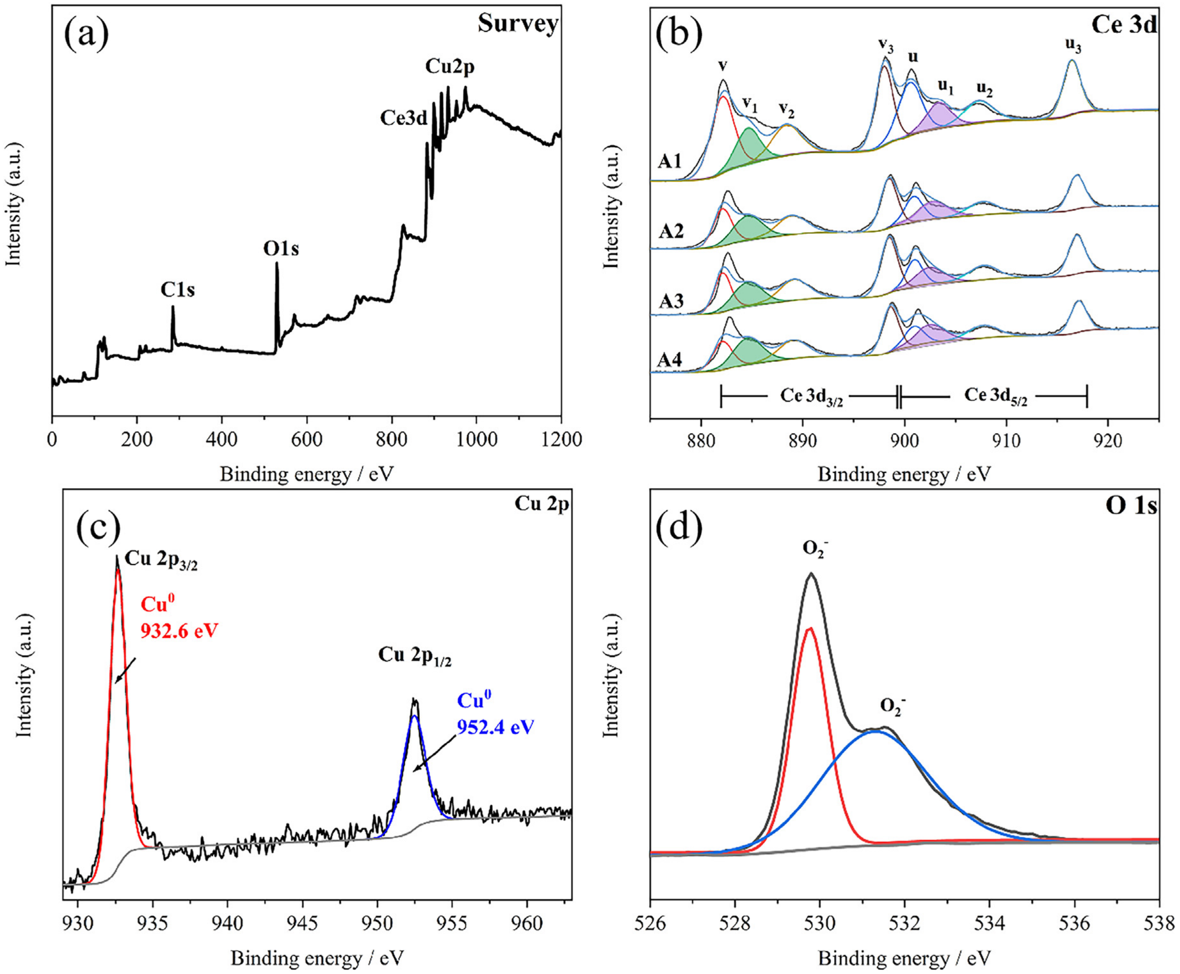

Fig. 4. XPS spectrum of Cu/CeO_2 (a), high-resolution XPS spectra of Ce 3d (b), Cu 2p (c) and O 1s (d).

with the increase of copper, the corresponding fuel will also increase, leading to a further increase in reducing gas and the concentration of trivalent cerium.

$$CeO_2 + xCO = CeO_{2-x} + xCO_2 \quad (7)$$

The Cu 2p XPS fine spectrum of the sample is shown above (Fig. 4(c)), and a split peak fit to it reveals binding energy peaks near 932.6 eV (Cu $2p_{3/2}$) and 952.4 eV (Cu $2p_{1/2}$) corresponding to zero-valent metallic copper.[36,37] It is noteworthy that the Cu 2p XPS fine spectrum of the sample fails to observe a clear satellite peak corresponding to Cu^{2+}, implying that the sample does not have a significant oxidation state on the surface and only exhibits the characteristics of zero-valent metallic copper. The core-level XPS spectra of O 1s of composite A4 are shown in Fig. 4(d), there are two peaks at 529.2 and 531.3 eV in the samples, which are attributed to O_2^- confined by Ce^{4+} ions and O_2^- ions to Ce^{3+} ions, respectively.[38] These findings are also in accord with the work of Zheng et al.[39]

To determine the valence state of Cu, the samples were subjected to Auger electron analysis. Fig. S3 in S.I. shows the Cu LMM Auger signals spectrum of sample A4, which was fitted to the split peaks, and it is found that the fitted peak near the kinetic energy of 918.2 eV corresponds to copper metal.[40] This corresponds well to Eq. (4), where CuO is completely reduced to Cu.

3.2. Photocatalytic characterization

The optical properties of materials directly affect their photocatalytic activity. The results of UV visible absorption spectra are illustrated in Fig. 5, it can be found that all samples have the light response in the visible-light region $\lambda = 400–600$ nm). Compared with the synthesized CeO_2, the Cu/CeO_2 composite has higher absorption intensity in the visible region, and the redshift trend of the absorption edge increases with the increase of Cu content. The trend of the band gap of the synthesized products is shown in the Tauc diagram in Fig. 5(b), and it is obvious that the band gap value decreases with the increase of Cu content. The narrowing of the band gap indicates the electronic interaction between Cu and CeO_2. These factors contribute to the enhancement of visible-light absorption and the formation and transfer of photogenerated charges and carriers at the interface.

As shown in Fig. 6(a), photoluminescence (PL) measurements were executed to determine the conveyance of photo-electrons and holes. It is well known that PL intensity is associated with the recombination of photogenerated charges in semiconductors. Compared with CeO_2, Cu/CeO_2 nanomaterials exhibits a lower absorption peak at 300–700 nm under the excitation of 350 nm, showing that the combination of Cu could restrict the fluorescence of CeO_2. The lower PL spectrum intensity implies that the electron-

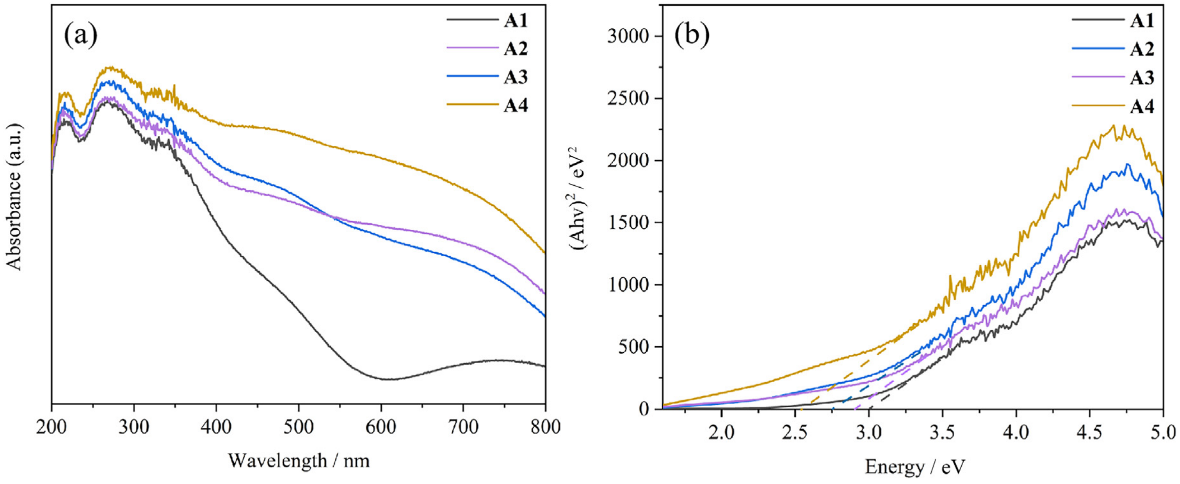

Fig. 5. (a) UV-vis diffuse reflectance spectra (DRS) of all CeO_2 and Cu/CeO_2 composites; (b) Tauc's plot of CeO_2 and Cu/CeO_2.

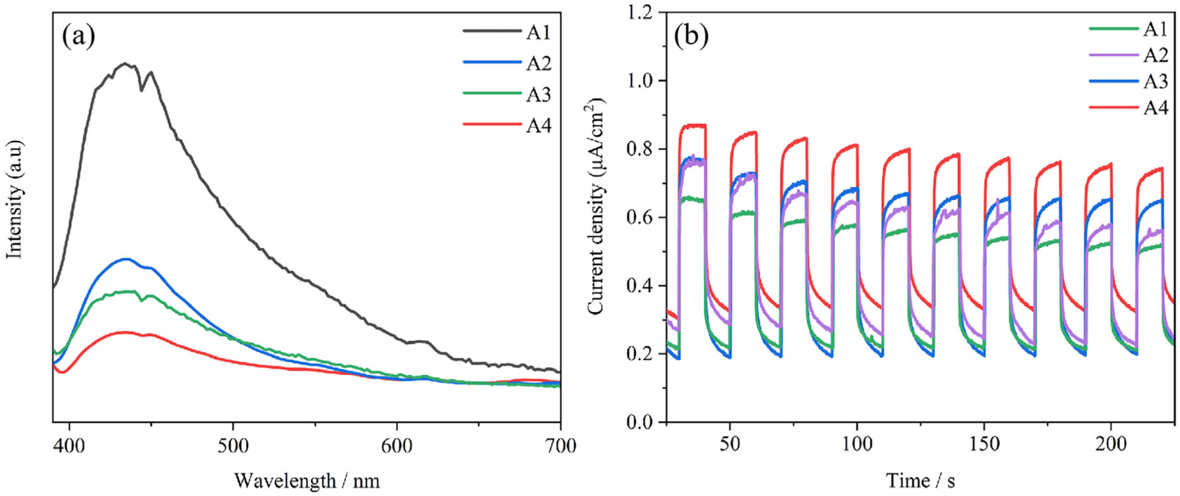

Fig. 6. (a) PL spectra of all CeO_2 and Cu/CeO_2 composites; (b) Photocurrent response of CeO_2, 10 wt% Cu/CeO_2, 20 wt% Cu/CeO_2 and 30 wt% Cu/CeO_2.

hole recombination rate is reduced, which means a longer lifetime of the photogenerated carriers.

On the other hand, the photocurrent density test is an effective method to study the transportability of photo-generated electrons and holes in photocatalytic reactions. In general, the stronger the photocurrent response of the photocatalytic material, the better the separation of photogenerated carriers and the lower the degree of recombination. As shown in Fig. 6(b), the transient and uniform photocurrent response of CeO_2, Cu/CeO_2 composites can be observed with the opening and closing process of light. Among all the samples, A4 exhibited the highest photocurrent, successively followed by A3 and A2, which ended with the as-synthesized CeO_2 sample. Each of the composite materials introduced with Cu element has a higher photocurrent than that of the as-synthesized CeO_2. The above results further demonstrate that the introduction of the Cu element significantly improves the broad charge life and separation efficiency of CeO_2. These photoelectrochemical results are in good accordance with the photocatalytic performance and the PL test.

The photocatalytic activities of all the as-prepared samples were assessed by the degradation of MO dye pollutant molecules in aqueous media under ultraviolet-visible irradiation. From Fig. 7(a), it can be seen that after 120 min, the photocatalytic efficiency of Al is 21.98%, and the introduction of Cu increases the degradation efficiency. In particular, the photocatalytic efficiency of 30 wt% Cu (A4) composites exhibits the best performance (95.99%), which is about 4.3 times that of CeO_2 (A1) at the same time (120 min). MO was almost not degraded with the absence of photocatalyst under ultraviolet-visible irradiation. To study the kinetic relationship of photocatalytic degradation, the relationship between $\ln(A_i/A_0)$ and radiation time was plotted based on the photocatalytic experimental data (Fig. 7(b)). The values of $\ln(A_i/A_0)$ can be calculated from the photocatalytic performance experimental values. The first-order kinetic reaction line was fitted, and the first-order rate constant (k) was estimated by the relationship of $-\ln(A_i/A_0) = kt$.[41] The more thoroughly MO is degraded, the higher the k value is.[42] The estimated pseudo-first-order rate constants (k) are 0.0015 (min^{-1}), 0.0051 (min^{-1}), 0.0119 (min^{-1}) and 0.0215 (min^{-1}) for A1, A2, A3 and A4 nanoparticles, respectively. With the addition of Cu, the rate constant increases gradually, and the rate constant for the 30 wt% Cu/CeO_2 sample is about 4.3 times that of CeO_2. These results implied that the presence of Cu can improve the light absorption intensity, effectively separate the photogenerated electron-hole pairs and prolong the charge carrier lifetime, thus significantly improve the photocatalytic performance.

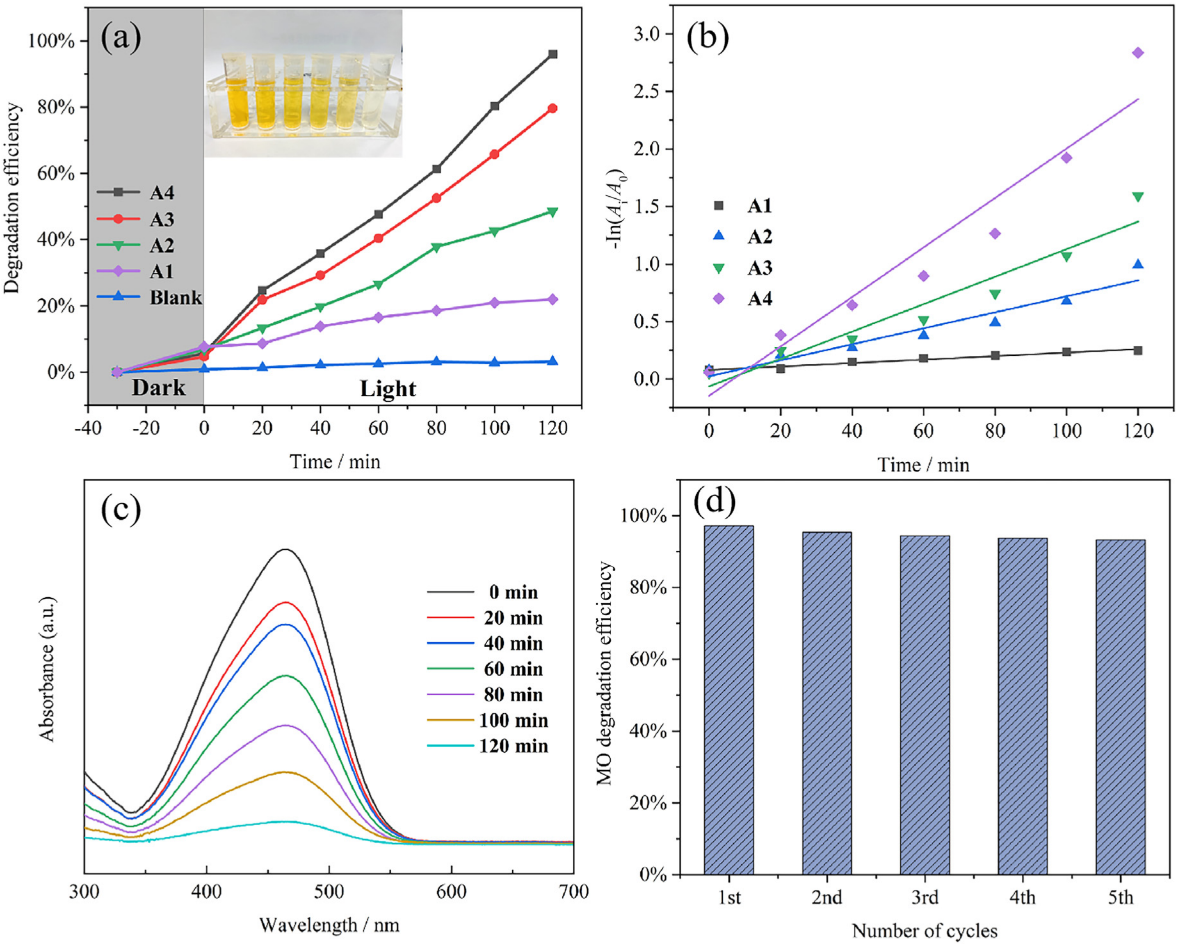

Fig. 7. Time profiles of photocatalytic degradation of MO over the as-prepared samples and inset shows the color change of MO for the Cu-30% composite as a photocatalyst (a) and kinetic data fitting for the degradation of MO (b); UV-Vis absorption spectra of MO solutions containing (c) and cycle test of Cu-30 wt% composite (d).

As shown in Fig. 7(c), the photocatalytic activity of the 30 wt% Cu/CeO_2 composite was further examined by the degradation degree of methyl orange dye aqueous solution under the irradiation of xenon lamp. Contaminant concentrations were measured at regular intervals (20 min) and absorbance intensities are compared. The major absorption band of methyl orange at around 464 nm faded gradually with time under simulated visible light irradiation in the existence of A4 sample, which indicates the degradation of MO dye. In addition, from the perspective of practical application, the stability of as-prepared samples is noteworthy besides the photocatalytic activity. Therefore, the reusability of 30 wt% Cu composites photocatalyst was evaluated by recirculation experiments. As depicted in Fig. 7(d), the 30 wt% Cu composites still keep excellent degradation efficiency of 93.3% after 5 cycles, which proves the photostability of the as-prepared photocatalyst.

To further study the photocatalytic mechanism, the trapping experiments of reactive species were conducted to figure out the main active species. The trapping experiment is similar to the photocatalysis experiment, and isopropyl alcohol (IPA),[43] 1,4-benzoquinone (BQ)[44] and ammonium oxalate (AO)[45] were added into MO aqueous solution as the effective scavengers to clear $\cdot OH$, $\cdot O_2^-$ and h^+, respectively. Fig. 8(a) depicted that the addition of the scavengers decreases the degradation efficiency of MO, which is more so for BQ and AO (the photocatalytic efficiency is only 15.1% and 11.3%). Moreover, when IPA is added, there is no obvious effect on the degradation of MO (89.4%). In a nutshell, $\cdot O_2^-$ and h^+ species serve a significant function in the photocatalytic degradation of MO.

Based on the experimental results and characterizations, a hypothesized mechanism for enhanced photocatalysis of Cu/CeO_2 nanomaterials was proposed. As is known to all, photogenerated carriers are separated, electrons are introduced into the conduction band, and holes are formed in the valence band when the semiconductor is illuminated. The existing OVs can capture photogenerated electrons and convey the captured electrons to the adsorbent of the composites, thereby effectively suppressing the recombination of carriers and enhancing the photocatalytic activity. According to the above trapping experiments, the superoxide and holes play a significant function in the degradation of MO. And the existing OVs in CeO_2 can capture photo-generated electrons and convey the captured electrons to the adsorbent, thereby effectively suppress the recombination of carriers and enhancing the photocatalytic activity.

As shown in Fig. 8(b), the degradation process of organics on Cu/CeO_2 composites can be well described as follows: when the CeO_2 photocatalytic material is excited by ultraviolet-visible light with energy higher than the bandgap, electrons transfer from the valence band to the conduction band of cerium oxide, forming photogenerated electron-hole pairs (Eq. (8)). The photogenerated electrons and holes will be transferred to the surface of cerium oxide, and this process will be partially recombined by emitting photons (Eq. (9)). When the holes are trapped by organic

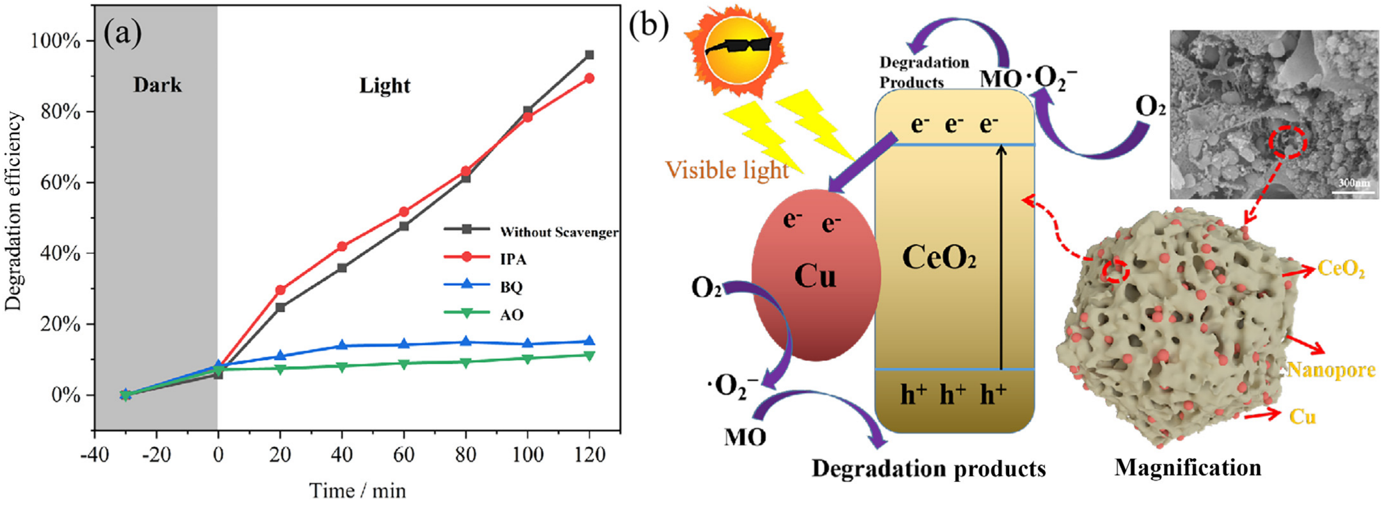

Fig. 8. (a) Effect of scavengers on the photocatalytic degradation of MO by the 30 wt% Cu composite; (b) schematic diagram of photocatalytic processes of Cu/CeO_2 nanomaterial.

compounds on the CeO_2 surface, the holes can directly degrade the organic compounds (as reaction (10)). In the photocatalytic reaction, the organic pollutant MO dye initially adsorbed on the catalyst surface and simultaneously it adsorbed the reactive oxygen species. The combination of electrons shuttled in the conduction band and dissolved oxygen in the solution produces superoxide radicals (as reaction (11)). Superoxide radicals can also directly react with MO to produce CO_2 and H_2O (as reaction (12)). The introduction of Cu plays an important role in the composite catalyst: Cu can be directly excited by light as an active species, the adsorbed reactant molecules trigger a resonance effect and generate high-energy electrons and holes for catalytic reactions (as reaction (13)). The photocatalytic degradation of organic with photogenerated electrons and holes is in the same route as the above reactions. The possible reactions about photocatalytic mechanism can be summarized as follows:

$$CeO_2 + h\nu\ (UV) \rightarrow CeO_2\ (e^- + h^+) \tag{8}$$

$$e^- + h^+ \rightarrow h\nu'\ (\text{recombination}) \tag{9}$$

$$h^+ + \text{organics} \rightarrow CO_2 + H_2O \tag{10}$$

$$e^- + O_2 \rightarrow \cdot O_2^- \tag{11}$$

$$\cdot O_2^- + \text{organics} \rightarrow CO_2 + H_2O \tag{12}$$

$$Cu + h\nu\ (\text{visible}) \rightarrow Cu\ (e^- + h^+) \tag{13}$$

Besides, Cu-modified CeO_2 receives photogenerated electrons and extends the life-span of charge carriers through surface plasmon resonance,[46] which leads to the improvement of the separation efficiency of electrons and holes and the enhancement of photocatalytic efficiency.

4. Conclusions

In the present study, Cu/CeO_2 catalyst was successfully synthesized in one step by the solution combustion combined with controlling the reaction atmosphere method. The as-prepared CeO_2 and Cu/CeO_2 composites exhibit nanoporous structure, in which the mesopores (diameter 10–17 nm) nest in the large pores (diameter 80–300 nm). The nanoporous structure retains the high specific surface area of nanocrystals (23.42 m^2/g) and provides more channels for mass transfer. The decoration of metal Cu on CeO_2 can generate more OVs in CeO_2, which will promote the electron transfer process, effectively prevent the charge carriers' recombination. As a result, transient photocurrent response and the PL spectrum demonstrate higher photo-induced charge separation efficiency in Cu/CeO_2 composites. The obtained Cu/CeO_2 photocatalysts exhibit enhanced degradation efficiency for MO (95.99%), which is about 4.3 times that of CeO_2 at the same time (120 min). Moreover, the Cu/CeO_2 composites also exhibit promising reusability and stability in five cycles (93.3%). It is expected that the Cu/CeO_2 nanomaterials could become a promising photocatalyst for energy conversion and environmental remediation. This work provides a simple and cost-effective method for producing metal-supported nano-porous oxides with high porosity and surface area.

Acknowledgements

This work was supported by the A. Varma Reaction Engineering Research Fund from the Davidson School of Chemical Engineering of Purdue University, and the Advanced Analysis & Computation Center of China University of Mining and Technology.

Appendix A. Supplementary data

Supplementary data to this article can be found online at https://doi.org/10.1016/j.jre.2022.02.013.

References

1. Gu P, Zhang S, Li X, Wang XX, Wen T, Jehan R, et al. Recent advances in layered double hydroxide-based nanomaterials for the removal of radionuclides from aqueous solution. *Environ Pollut*. 2018;240:493.
2. Kermani M, Izanloo H, Kalantary RR, Barzaki HS, Kakavandi B. Study of the performances of low-cost adsorbents extracted from rosa damascena in aqueous solutions decolorization. *Desalination Water Treat*. 2017;80:357.
3. Lee KC, Choo KH. Optimization of flocculation conditions for the separation of TiO_2 particles in coagulation-photocatalysis hybrid water treatment. *Chem Eng Process Process Intensif*. 2014;78:11.
4. Shen ZM, Wu D, Yang J, Yuan T, Wang WH, Jia JP. Methods to improve electrochemical treatment effect of dye wastewater. *J Hazard Mater*. 2006;B131:90.

5. Wetchakun N, Wetchakun K, Sakulsermsuk S. Influence of Fe dopant concentrations on physicochemical and photocatalytic properties of Bi_2WO_6/CeO_2 nanocomposites for rhodamine B degradation. *Int J Ind Chem*. 2020;11(3):161.
6. Montini T, Melchionna M, Monai M, Fornasiero P. Fundamentals and catalytic applications of CeO_2-based materials. *Chem Rev*. 2016;116(10):5987.
7. Shi XC, Yang JJ, Wen XT, Tian FL, Li CY. Oxygen vacancy enhanced biomimetic superoxide dismutase activity of CeO_2-Gd nanozymes. *J Rare Earths*. 2021;39(9):1108.
8. Phoka S, Laokul P, Swatsitang E, Promarak V, Seraphin S, Maensiri S. Synthesis, structural and optical properties of CeO_2 nanoparticles synthesized by a simple polyvinyl pyrrolidone (PVP) solution route. *Mater Chem Phys*. 2009;115(1):423.
9. Goharshadi EK, Samiee S, Nancarrow P. Fabrication of cerium oxide nanoparticles: characterization and optical properties. *J Colloid Interface Sci*. 2011;356(2):473.
10. Dhall A, Self W. Cerium oxide nanoparticles: a brief review of their synthesis methods and biomedical applications. *Antioxidants*. 2018;7(8):1.
11. Zou WX, Shao Y, Pu Y, Luo YD, Sun JF, Ma KL, et al. Enhanced visible light photocatalytic hydrogen evolution via cubic CeO_2 hybridized g-C_3N_4 composite. *Appl Catal B Environ*. 2017;218:51.
12. Wang YY, Wang F, Chen YT, Zhang DF, Li B, Kang SF, et al. Enhanced photocatalytic performance of ordered mesoporous Fe-doped CeO_2 catalysts for the reduction of CO_2 with H_2O under simulated solar irradiation. *Appl Catal B Environ*. 2014;147:602.
13. Zhong MH, Wang ZD, Dai D, Yang BZ, Zuo SX, Yao C, et al. Upconversion hollow nanospheres CeF_3 co-doped with Yb^{3+} and Tm^{3+} for photocatalytic nitrogen fixation. *J Rare Earths*. 2022;40(4):586.
14. Li B, Zhang BH, Guan QQ, Chen SS, Ning P. Activity of Ni/CeO_2 catalyst for gasification of phenol in supercritical water. *Int J Hydrogen Energy*. 2018;43(41), 19010.
15. Negi K, Umar A, Chauhan MS, Akhtar MS. Ag/CeO_2 nanostructured materials for enhanced photocatalytic and antibacterial applications. *Ceram Int*. 2019;45(16), 20509.
16. Navaneetha Pandiyaraj K, Vasu D, Ramkumar MC, Deshmukh RR, Ghobeira R. Improved degradation of textile effluents via the synergetic effects of Cu-CeO_2 catalysis and non-thermal atmospheric pressure plasma treatment. *Separ Purif Technol*. 2021;258(P2), 118037.
17. Zhang DS, Qian YL, Shi LY, Mai HL, Gao RH, Zhang JP, et al. Cu-doped CeO_2 spheres: synthesis, characterization, and catalytic activity. *Catal Commun*. 2012;26:164.
18. Ahmed N, Ahmed R, Rafiqe M, Baig MA. A comparative study of Cu-Ni Alloy using LIBS, LA-TOF, EDX, and XRF. *Laser Part Beams*. 2017;35(1):1.
19. Channei D, Jannoey P, Nakaruk A, Phanichphant S. Photocatalytic activity of Cu-doped cerium dioxide nanoparticles. *Key Eng Mater*. 2017;751:801.
20. Mousavi-Kamazani M, Azizi F. Facile sonochemical synthesis of Cu doped CeO_2 nanostructures as a novel dual-functional photocatalytic adsorbent. *Ultrason Sonochem*. 2019;58, 104695.
21. Zhang N, Liu SQ, Xu YJ. Recent progress on metal core@semiconductor shell nanocomposites as a promising type of photocatalyst. *Nanoscale*. 2012;4(7):2227.
22. Du X, Wang XH, Xiao Y. $Bi_5O_7NO_3$ and Ag/$Bi_5O_7NO_3$ composites: one-step solution combustion synthesis, characterization and photocatalytic properties. *CrystEngComm*. 2018;20(46):7536.
23. Wolf EE, Manukyan KV, Cross A, Roslyakov S, Rouvimov S, Rogachev AS, et al. Solution combustion synthesis of nano-crystalline metallic materials: mechanistic studies solution combustion synthesis of nano-crystalline metallic materials : mechanistic studies. *J Phys Chem C*. 2013;117(46), 24417.
24. Du XN, Liu Y, Wang XH, Feng JQ, Ren CF. Rapid preparation of α, β-Bi_2O_3 and α/β-Bi_2O_3 heterojunction with enhanced photocatalytic properties. *J Australas Ceram Soc*. 2019;55(1):71.
25. Jadhav LD, Patil SP, Chavan AU, Jamale AP, Puri VR. Solution combustion synthesis of Cu nanoparticles: a role of oxidant-to-fuel ratio. *Micro & Nano Lett*. 2011;6(9):812.
26. Yang XJ, Liu Y, Li J, Zhang YL. Effects of calcination temperature on morphology and structure of CeO_2 nanofibers and their photocatalytic activity. *Mater Lett*. 2019;241:76.
27. Lykaki M, Pachatouridou E, Iliopoulou E, Carabineiro SAC, Konsolakis M. Impact of the synthesis parameters on the solid state properties and the CO oxidation performance of ceria nanoparticles. *RSC Adv*. 2017;7(10):6160.
28. Miedziak PJ, Tang ZR, Davies TE, Enache DI, Bartley JK, Carley AF, et al. Ceria prepared using supercritical antisolvent precipitation: a green support for gold-palladium nanoparticles for the selective catalytic oxidation of alcohols. *J Mater Chem*. 2009;19(45):8619.
29. Deshpande S, Patil S, Kuchibhatla SV, Seal S. Size dependency variation in lattice parameter and valency states in nanocrystalline cerium oxide. *Appl Phys Lett*. 2005;87(13):1.
30. Santos VP, Carabineiro SAC, Bakker JJW, Soares OSGP, Chen X, Pereira MFR, et al. Stabilized gold on cerium-modified cryptomelane: highly active in low-temperature CO oxidation. *J Catal*. 2014;309:58.
31. Zhang XL, Li K, Shi WY, Wei CH, Song XP, Yang S, et al. Baize-like CeO_2 and NiO/CeO_2 nanorod catalysts prepared by dealloying for CO oxidation. *Nanotechnology*. 2017;28(4):11.
32. Kato S, Ammann M, Huthwelker T, Paun C, Lampimäki M, Lee MT, et al. Quantitative depth profiling of Ce^{3+} in Pt/CeO_2 by *in situ* high-energy XPS in a hydrogen atmosphere. *Phys Chem Chem Phys*. 2015;17(7):5078.
33. Zhou GL, Xie FQ, Deng LD, Zhang GZ, Xie HM. Supported mesoporous Cu/$CeO_{2-\delta}$ catalyst for CO_2 reverse water–gas shift reaction to syngas. *Int J Hydrogen Energy*. 2020;45(19), 11380.
34. Chen P, Liu HJ, Sun YJ, Li JY, Cui W, Wang LA, et al. Bi metal prevents the deactivation of oxygen vacancies in $Bi_2O_2CO_3$ for stable and efficient photocatalytic NO abatement. *Appl Catal B Environ*. 2020;264, 118545.
35. Ashok A, Kumar A, Tarlochan F. Surface alloying in silver-cobalt through a second wave solution combustion synthesis technique. *Nanomaterials*. 2018;8(8):1.
36. Sener ME, Sathasivam S, Palgrave R, Quesada Cabrera R, Caruana DJ. Patterning of metal oxide thin films using a H_2/He atmospheric pressure plasma jet. *Green Chem*. 2020;22(4):1406.
37. Fan Z, Baranovas G, Yu HA, Szczęsny R, Liu WR, Gregory DH. Ultra-rapid synthesis of the $MgCu_2$ and Mg_2Cu Laves phases and their facile conversion to nanostructured copper with controllable porosity; an energy-efficient, reversible process. *Green Chem*. 2021;23(18):6936.
38. Sharma JK, Srivastava P, Ameen S, Akhtar MS, Sengupta SK, Singh G. Phytoconstituents assisted green synthesis of cerium oxide nanoparticles for thermal decomposition and dye remediation. *Mater Res Bull*. 2017;91:98.
39. Zheng XH, Li YL, Liang SJ, Yao Z, Zheng Y, Shen LJ, et al. Promoting effect of Cu-doping on catalytic activity and SO_2 resistance of porous CeO_2 nanorods for H_2S selective oxidation. *J Catal*. 2020;389:382.
40. Tong LH, Ren LT, Fu A, Wang DF, Liu LQ, Ye JH. Copper nanoparticles selectively encapsulated in an ultrathin carbon cage loaded on $SrTiO_3$ as stable photocatalysts for visible-light H_2 evolution: via water splitting. *Chem Commun*. 2019;55(86), 12900.
41. Ayodhya D, Veerabhadram G. Green synthesis of garlic extract stabilized Ag@CeO_2 composites for photocatalytic and sonocatalytic degradation of mixed dyes and antimicrobial studies. *J Mol Struct*. 2020;1205, 127611.
42. Zhang J, Wang B, Cui H, Li C, Zhai JP, Li Q. Synthesis of CeO_2/fly ash cenospheres composites as novel photocatalysts by modified pyrolysis process. *J Rare Earths*. 2014;32(12):1120.
43. Gadhi TA, Hernández-Gordillo A, Bizarro M, Jagdale P, Tagliaferro A, Rodil SE. Efficient α/β-Bi_2O_3 composite for the sequential photodegradation of two-dyes mixture. *Ceram Int*. 2016;42(11), 13065.
44. Huang YK, Kang SF, Yang Y, Qin HF, Ni ZJ, Yang SJ, et al. Facile synthesis of Bi/Bi_2WO_6 nanocomposite with enhanced photocatalytic activity under visible light. *Appl Catal B Environ*. 2016;196:89.
45. Xiao X, Hu RP, Tu SH, Zheng CX, Zhong H, Zuo XX, et al. One-pot synthesis of micro/nano structured β-Bi_2O_3 with tunable morphology for highly efficient photocatalytic degradation of methylparaben under visible-light irradiation. *RSC Adv*. 2015;5(48), 38373.
46. Tang YX, Wee PX, Lai YK, Wang XP, Gong DG, Kanhere PD, et al. Hierarchical TiO_2 nanoflakes and nanoparticles hybrid structure for improved photocatalytic activity. *J Phys Chem C*. 2012;116(4):2772.